JOURNAL OF GUIDANCE, CONTROL, AND DYNAMICS
Vol. 17, No. 5, September–October 1994

Stability of Spinning Spacecraft Containing Shallow Pool of Liquid Under Thrust

A. C. Or*
University of California, Los Angeles, Los Angeles, California 90024
and
A. D. Challoner†
Hughes Aircraft Company, El Segundo, California 90245

A well-known flight nutation instability observed with spinning spacecraft under the thrust of a solid rocket motor is examined. A shallow pool of molten slag trapped in the aft motor chamber is represented by a linearized hydrodynamic coupled finite element model. The frequency of the dominant retrograde "swirl" mode of the uncoupled liquid is found to intersect the spacecraft nutation frequency during the anomalous flight and is the suspected cause of instability. With no effects of internal gas flow the coupled model predicts the onset of instability only at the very end of the burn. However, if the equilibrium liquid shape is deformed slightly more outboard, as suggested by a previously predicted recirculating gas flow in the motor chamber, then the model is capable of matching the onset of nutation growth observed in flight. The subsequent nutation growth amplitude profile is also matched. However, the nutation frequency of the linear model deviates from the flight value as the burn progresses. For a prolate spinner, high spin speed, low thrust and large slag axial offset are the conditions for instability; for an oblate spinner the destabilizing conditions are opposite.

Introduction

ANOMALOUS attitude instabilities of a number of spin-stabilized spacecraft upper stages have stimulated several interesting studies[1–9] for the cause. Of the numerous theories advanced it seems that only two have the potential of matching the type of motions observed in flight. These are the gas dynamics theory and the liquid slag theory.

The gas theory proposed to explain the Perigee Assist Motor D (PAM-D) coning anomaly[2] suggests that the gas flow has a number of inertial modes that are driven by vehicle nutation. A major difficulty, also recognized by others, is that the inertial mode theory of a spinning liquid in a closed container[10] was applied to the flow-through situation of a very stiff gas jet. With outflow, the boundary conditions for the problem are greatly altered. Also, the apparent good correlation between this theory and the Westar IV flight data was the result of an unfortunate coding error, which only came to light after publication. Recently, Misterek et al.[3] performed a numerical simulation on the coupled nutation response of the gas jet based on the direct solution of the Navier-Stokes equations and associated boundary conditions. They concluded that there is no destabilizing moment similar to that observed in the PAM toward the end of burn. These authors did observe a significant decrease in the jet-damping moment. There is up to 60% decrease from that predicted by the classical theory. The jet-damping moment is due solely to the difference in the angular momentum influx (from solid propellant) and outflux (at nozzle exit) and has nothing to do with resonance locking (i.e., the phenomenon wherein two closely tuned resonators interact or "lock together" and oscillate at a common frequency with one stable and one unstable system mode, e.g., wing flutter arising from aerodynamically coupled wing bending and twist modes).

The second theory has also stimulated a number of investigations, mostly using simple mechanical models, in which the liquid motion is represented by that of a point mass. Mingori and Yam's[4] model was extended by Or[5] to include the effect of spin and to incorporate other different kinematic constraints. These models treat the onset stability problem and are all capable of reproducing the flight anomalous time response by tuning only a few major parameters. The models, however, are deficient as the nutation angle exceeds a few degrees. As noted in Or's paper, the discrepancy is due to the mismatch of the strength and relative magnitudes of the cross-coupling terms rather than to the absence of nonlinearity. Recently, Cochran and Kang[6,7] include also the nonlinear response in a similar model, which appears to produce motions similar to those observed in the flight under some restrictions. Recently, the occurrence of molten slag during solid rocket burn has gained more evidence. Indeed, some slag motions were even videoed through testing processes. The slag accumulation is quite a complex process. Meyer[11] has developed a model for the estimation of the slag transport in the motor chamber. He suggested that the trapped slag mass is proportional to the fourth power of the motor diameter.

The point-mass mechanical models are revealing. Several major findings are worth noting. First, the onset of the anomaly appears to be a well-defined linear process. Thus it seems that onset prediction is of the most crucial importance in this case. Second, the instability can occur when the point mass lies aft of the spacecraft center of mass. Typically, for such a configuration, the thrust, or gravity force, is stabilizing, as inferred from the minimum potential energy principle. The instability would be less surprising, however, were it to occur when the point mass is above the center of mass, where gravity destabilizes. In the planar pendulum model Or[5] considered, there are two competing effects: the stabilizing thrust force and the destabilizing centrifugal force (the spin). That the centrifugal effect plays a destabilizing role is not all that surprising, since it is well known that the spin kinetic energy for a prolate spinner ($\sigma < 1$) is at a maximum for a given angular momentum. The thrust produces stabilizing effects. It may, however, contribute toward the instability by shifting the frequency and phasing condition in the direction of the locking. The instability occurs typically at a high Froude number. In Or's model, the combination of high spin and low thrust are inherently dangerous. In fact, judging qualitatively from the previous flight experience, the destabilizing spin and stabilizing thrust for a prolate spinner appear to be rather consistent. The role of spin and thrust, however, reverses as σ exceeds 1 (an oblate spinner). On the other hand, the Mingori-type model, or analogously, Or's spherical pendulum model and some other similar models currently being used for flight predictions, has spin effects detached from the

---

Received July 13, 1992; revision received Jan. 19, 1994; accepted for publication Jan. 23, 1994. Copyright © 1994 by Hughes Aircraft Company. Published by the American Institute of Aeronautics and Astronautics, Inc., with permission.

*Research Engineer, Department of Mechanical, Aerospace and Nuclear Engineering.

†Scientist/Engineer, Hughes Space and Communications. Member AIAA.

pivot. That is, the point mass is not subjected to Coriolis force and only responds to the precession forcing. Even though the model can be tuned to produce nutation resonance divergence by utilizing the thrust as the destabilizing force, it appears for one reason or another that these models are somewhat deficient in matching observations. The nutation instability in the analogs of the spherical pendulum model does not depend on whether the spinning body is prolate or oblate. The dedamping time constant and the stability limit are not functions of σ explicitly.

Nutation amplification of a prolate spinning body due to nutation and liquid inertial mode locking is well established both theoretically and experimentally. In Ward's experiment, reported by Stewartson,[12] the nutational vibration was so intense that it almost broke the gimbal bearing. McIntyre and Tanner,[13] developed a finite element hydrodynamic model for the PAM-D problem using their eigenmode approach. However, no instability was found when the liquid was placed below the spacecraft center of mass. The numerical experiment led McIntyre and Tanner to argue based on a heuristic mechanism why the slag cannot cause nutational instability in the case of the PAM-D spacecraft. Their study showed that the thrust is stabilizing. Their pioneering work provided the motivation for our present study. We point out, however, that the authors treat the coupled problem by a method of eigenmode expansion similar to the one described by Greenspan[10] (see pp. 68–78). This method is strictly valid only for a liquid in a closed container without a free surface. A strictly correct procedure would require the velocity and pressure fields to have different modal coefficients. In our method,[14] the velocity field is eliminated in favor of the pressure and a direct solution is sought numerically for the coupled problem rather than for an expansion based on the free-liquid eigenmodes.

Recently, Staunton and Mingori[9] approached the PAM-D problem with a direct analytic solution reminiscent of the work on the spinning top by Stewartson.[12] It naturally required some rather restrictive assumptions, e.g., one-dimensional flow. However, it has defined a basic two-mode model for the slag that shows the possibility for locking with vehicle nutation under certain parametric conditions, e.g., low thrust, but not under conditions similar to actual flight. This two-mode slag model is qualitatively in agreement with the two dominant modes found in this work and in earlier investigations at Hughes. The crucial issue is to compute the quantitatively correct frequency and coupling under actual flight conditions and the difficulty is that the shape and quantity of slag vs time are highly unknown.

Our goal is to more extensively assess the various possibilities given the flight specifications that can produce divergent motions similar to those observed in flight using less retrictive hydrodynamic modeling or spacecraft coupling assumptions. The comprehensive parametric stability analysis developed for Or's[5] pendulum study provides a framework for this study. The mathematical formulation also allows for distortion of the liquid shape due to the chamber gas flow. An analysis of the equilibrium spin and thrust condition is first provided that raises the distinct possibility of instability. This is followed by results with equilibrium surface distortion due to gas flow that show onset of instability and divergent nutation amplitude behavior similar to the flight case, although the predicted nutation frequency begins to deviate from the flight value as the burn progresses.

Mathematical Formulation

Consider an axisymmetric free-flying rigid body that rotates about its axis of symmetry L_z (see Fig. 1). The body contains an on-axis spherical cavity whose center distance from the dry-body center of mass can be varied. The body is under the action of a constant axial force. The cavity is assumed to contain a shallow pool of liquid. The liquid is bounded by the spherical casing and by the submerged nozzle. Due to the effect of the gas flow generated under the burn, the entrapped liquid shape cannot be purely determined by thrust and centrifugal forces, i.e., hydrostatic balance. In this study, we assume the free surface to be paraboloid. A shape parameter β is introduced. The shape can be regarded as the lowest order approximation of the actual equilibrium shape. The case of hydrostatic balance corresponds to $\beta = 1$. The liquid is also assumed to be incompressible and inviscid, whereas its equilibrium flow field acquires rigid rotation.

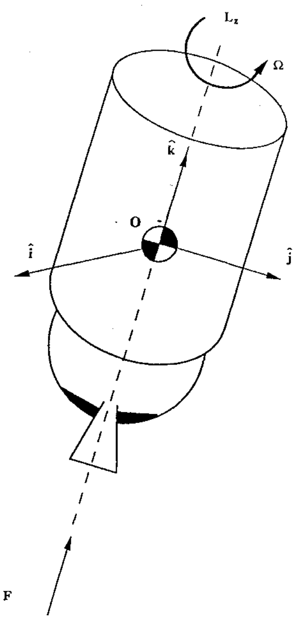

Fig. 1 Spacecraft geometry.

Referring to Fig. 1, the dry-body center of mass O is chosen to be the origin of the body-fixed analyst's frame defined by an orthogonal triad of unit vectors $[\hat{i}, \hat{j}, \hat{k}]$. The rectilinear motion of the system center of mass with body-fixed thrust F is,

$$\ddot{\boldsymbol{R}}_0 = a\hat{k}, \qquad a = \frac{F}{m+M} \tag{1}$$

where m is the mass of liquid and M is the mass of the rigid body. In this problem, to first-order, we cannot distinguish acceleration of the dry body from that of the total center of mass; the first-order perturbations from the molten slag are coupled by a very small liquid mass ratio, typically less than 0.01.

The primitive form of angular momentum balance of the system is given by

$$(\dot{\boldsymbol{h}}_d + \boldsymbol{\omega} \times \boldsymbol{h}_d) + \frac{\mathrm{d}}{\mathrm{d}t}\int_V \rho \boldsymbol{r} \times \boldsymbol{v}\,\mathrm{d}V = \boldsymbol{T} + \ddot{\boldsymbol{R}}_0 \times \int_V \rho \boldsymbol{r}\,\mathrm{d}V,$$

$$\boldsymbol{h}_d = \int_{V_d} \rho_d \boldsymbol{r} \times (\boldsymbol{\omega} \times \boldsymbol{r})\,\mathrm{d}V \tag{2}$$

where $\boldsymbol{h}_d$ is the dry body's angular momentum relative to O, ρ_d and V_d are, respectively, the density and the volume of the rigid body, and ρ and V are, respectively, the density and the perturbed volume of the liquid. The integral of the left-hand side of Eq. (2) represents the time rate of change of the liquid angular momentum, where $\boldsymbol{v}$ is the liquid inertial velocity field with respect to the body frame, $\boldsymbol{T}$ is the external moment applied to the body, and the integral term on the right-hand side arises from the fact that the origin is noninertial. We define equilibrium rate and velocity as

$$\omega_0 = \Omega\hat{k}, \qquad v_0 = \Omega \boldsymbol{k} \times \boldsymbol{r} \tag{3}$$

where Ω is the spin rate of the rigid body and the liquid. When the motion is slightly perturbed by a transverse body rate about the equilibrium, we have

$$\omega = \Omega\hat{k} + \omega_T, \qquad \boldsymbol{v} = (\Omega \boldsymbol{k} + \omega_T) \times \boldsymbol{r} + \boldsymbol{u} \tag{4}$$

where both ω_T and $\boldsymbol{u}$ are considered as perturbation quantities. The liquid velocity $\boldsymbol{v}$ and volume integrals in Eq. (2) can be replaced by a single surface integral using Eqs. (3) and (4)[12,14] and the definition of pressure in the liquid Euler equation defined in the next paragraph,

$$(\dot{\boldsymbol{h}}_d + \boldsymbol{\omega} \times \boldsymbol{h}_d) = \boldsymbol{T} + \int_{S_w} p \boldsymbol{r} \times \boldsymbol{n}\,\mathrm{d}S \tag{5}$$

where S_w stands for the wall surface. Equivalently, the system momentum balance can be developed in terms of liquid perturbation velocity $\boldsymbol{u}$ using Eqs. (2–4).[13]

The linearized inviscid Euler equation for the liquid slag in the body frame is

$$\partial_t \boldsymbol{u} + 2\Omega\hat{\boldsymbol{k}} \times \boldsymbol{u} + \nabla P = \boldsymbol{G} \tag{6}$$

where

$$P = (p - p_0)/\rho + a(z - z_0), \qquad z_0 = z_b + \Omega^2 r^2/2a \tag{6a}$$

$$\boldsymbol{G} = -\{\dot{\boldsymbol{\omega}}_T \times \boldsymbol{r} + \Omega[\hat{\boldsymbol{k}} \times (\boldsymbol{\omega}_T \times \boldsymbol{r}) + \boldsymbol{\omega}_T \times (\hat{\boldsymbol{k}} \times \boldsymbol{r})]\} \tag{6b}$$

where the "dynamic" pressure P is also referred to as the acceleration potential; p_0 is a reference pressure, which is a constant of integration; and z_b is a reference height. See, e.g., Refs. 13 or 14 for more details. Liquid continuity or mass conservation in body coordinates is expressed as

$$\nabla \cdot \boldsymbol{u} = 0 \tag{7}$$

and the natural boundary conditions governing the liquid motions are

$$\begin{aligned} \boldsymbol{u} \cdot \hat{\boldsymbol{n}} &= 0 && \text{on} \quad S_w \\ p = p_g &= p_s + \tilde{p}(r, z) && \text{on} \quad S_f \end{aligned} \tag{8}$$

where S_f stands for free surface and p_g stands for the gas pressure. Thus the free-surface boundary condition of the liquid is the continuity of pressure across the surface.

For convenience, we separate p_g into the sum of a constant or static pressure p_s and a spatially varying pressure $\tilde{p}$ that is in general a function of r and z. We assume that $p_s \gg \tilde{p}$ but the gradient of $\tilde{p}$ is on the same order as the two static forces acting on the liquid. Without relative mean flow of the gas, the static pressure gradient of the gas is so small that p_g can be assumed to be constant so that we have $\tilde{p} \approx 0$. In this case, the equilibrium free surface is determined solely by the two static forces, such that the surface is normal to the resultant of the forces. With relative gas mean flow, the liquid free surface is again normal to the resultant forces, but now the mean flow pressure gradient has to be taken into account. Now, we equate the two expressions of p in Eqs. (6a) and (8). We obtain the reference pressure and the equilibrium free-surface height as

$$p_0 = p_s, \qquad z = z_b + \Omega^2 r^2/2a - \tilde{p}/\rho$$

In general, $\tilde{p}$ cannot be obtained without solving a two-phase flow problem. To simplify the problem for the PAM-D simulation, the only salient assumption we shall make in our analysis is that $\tilde{p}$ is a function of r only and only the term proportional to r^2 is kept. We can rewrite the above expression as

$$z = z_b + \beta\Omega^2 r^2/2a \tag{9}$$

We refer to β as a shape parameter. The equilibrium, the liquid shape without gas flow, is given by Eq. (6a) and corresponds to the above expression with $\beta = 1$. In the section on nutational stability with recirculating gas flow, we argue that, due to some evidence of a recirculation vortex flow in the aft region of the chamber, we may expect to have an equilibrium liquid shape corresponding to $\beta > 1$. The perturbed free-surface deformation is given by the following kinematic equation, which relates the surface perturbation velocity $\boldsymbol{u}$ to the Lagrangian displacement $\boldsymbol{\xi}$

$$\frac{\mathrm{D}}{\mathrm{D}t}\boldsymbol{\xi} = \boldsymbol{u}, \qquad \text{on} \qquad S_f$$

In the following, we eliminate the velocity field in favor of a higher order scalar system in P. We take partial derivatives of Eq. (6) with respect to time and then eliminate the Coriolis term by substituting the original equation (6) into the equation, and finally, we have an expression for the velocity field $\boldsymbol{u}$ in terms of P,

$$\partial_t\left(4\Omega^2 + \partial_{tt}^2\right)\boldsymbol{u} = \boldsymbol{L}(\nabla P - \boldsymbol{G}) \tag{10}$$

where $\boldsymbol{L}$ is a differential operator defined as

$$\boldsymbol{L} = \partial_t(-\partial_t + 2\Omega\hat{\boldsymbol{k}} \times) - 4\Omega^2\hat{\boldsymbol{k}}\hat{\boldsymbol{k}} \tag{11}$$

From Eq. (11), the continuity equation (7) immediately gives the traditional Poincaré equation for a spinning liquid,

$$\nabla \cdot [\boldsymbol{L}(\nabla P - \boldsymbol{G})] = 0 \qquad \text{or} \qquad \partial_{tt}^2 \nabla^2 P + 4\Omega^2(\boldsymbol{k} \cdot \nabla)^2 P = 0 \tag{12}$$

noting that $\nabla \cdot \boldsymbol{LG} \equiv 0$. By taking the dot product of the right side of Eq. (10) with $\hat{\boldsymbol{n}}$, the outward normal at the wall, the coupled wall boundary condition $\boldsymbol{u} \cdot \hat{\boldsymbol{n}} = 0$ becomes, in terms of our chosen variables P and $\boldsymbol{G}$,

$$\hat{\boldsymbol{n}} \cdot \boldsymbol{L}(\nabla P - \boldsymbol{G}), \qquad \text{on} \qquad S_w \tag{13}$$

The coupled free-surface condition is similarly derived from

$$\frac{\mathrm{D}}{\mathrm{D}t}(p - p_g) = 0 \qquad \text{on} \qquad S_f$$

After differentiating the expression, linearizing, and using the expression in Eq. (9), we obtain

$$\partial_t P = (a^2 + \beta^2\Omega^4 r^2)^{1/2}\boldsymbol{u} \cdot \hat{\boldsymbol{n}} \qquad \text{on} \qquad S_f \tag{14}$$

Although the equilibrium shape of the free surface is determined by the balance of a number of forces, the linearized dynamic boundary condition of a point on the surface is determined by a balance between the local temporal rate of change of pressure and the convective change along the gradient of the static head. Again, using Eq. (10) to eliminate $\boldsymbol{u} \cdot \hat{\boldsymbol{n}}$, we have the coupled free-surface boundary condition

$$\partial_{tt}^2(4\Omega^2 + \partial_{tt}^2)P = (g^2 + \beta^2\Omega^4 r^2)^{1/2}\hat{\boldsymbol{n}} \cdot \boldsymbol{L}(\nabla P - \boldsymbol{G}), \quad \text{on} \quad S_f \tag{15}$$

In component form, the system angular momentum equation (5) can be explicitly written as

$$A\dot{\omega}_1 + (C - A)\Omega\omega_2 = \int_{S_w}(yn_z - zn_y)P\,\mathrm{d}S \tag{16a}$$

$$A\dot{\omega}_2 - (C - A)\Omega\omega_1 = -\int_{S_w}(xn_z - zn_x)P\,\mathrm{d}S \tag{16b}$$

where A and C are respectively the transverse and axial moments of inertia of the dry body; the rigid liquid reactions are naturally contained in the right-hand pressure integrals. The circular symmetry of the problem permits us to reduce the three-dimensional problem to a two-dimensional form by using both the cylindrical coordinates and the complex notation for the variables. In cylindrical coordinates (r, θ, z), we define

$$x + iy = re^{i\theta}, \quad \omega_1 + i\omega_2 = \omega, \quad n_x + in_y = n = n_r e^{i\theta} \tag{17}$$

Further reduction of parameters is made possible by the nondimensionalization. Here we use Ω^{-1} as the scale of time and R as the scale of length, where R is radius of the motor chamber. In complex form, the angular momentum equation becomes

$$[\dot{\omega} - i(\sigma - 1)]\omega = \epsilon\hat{T}_l, \tag{18}$$

where

$$\hat{T}_l = i\int_{S_w}(zn_r - rn_z)e^{i\theta}P\,\mathrm{d}S,$$

$$z = z_b + \beta Fr\, r^2/z.$$

The nondimensional P represents $\rho\Omega^2 R^2 P$ in the dimensional case. The major parameters in the equation are defined as

$$Fr = \Omega^2 R/a, \qquad \epsilon = \rho R^5/A, \qquad \sigma = C/A \tag{19}$$

The Froude number Fr measures the relative importance between the centrifugal force and the axial force; liquid inertial fraction ϵ measures the transverse inertia of the liquid relative to the transverse inertia of the rigid body about the origin; and inertia ratio σ measures the dry rigid body's gyroscopic stiffness. Next, we notice that the integral in Eqs. (18) is nonvanishing only for waves with an azimuthal wavenumber of 1. In complex form ω becomes

$$\omega = \hat{\omega} e^{i\lambda t} \tag{20a}$$

The only modes that need to be considered for the dependent variable have the form

$$P(r,\theta,z) = \tfrac{1}{2}\left[\hat{P}(r,z)e^{-i\theta+i\lambda} + \text{complex conjugate}\right] \tag{20b}$$

We also rewrite T_l as $i\hat{T}_l e^{i\lambda t}$. Now after substituting Eqs. (17), (20a), and (20b) into Eq. (18) and reducing the integral dimension by integrating the azimuthal component, we obtain the angular momentum balance

$$[\lambda - (\sigma - 1)]\hat{\omega} = \epsilon T_l \tag{21}$$

where

$$T_l = \pi \int_{C_w} (zn_r - rn_z)\hat{P} r \, \mathrm{d}C$$

Substituting Eq. (20b) into Eq. (12), we obtain

$$L\hat{P} = \left[\lambda^2 \partial_r \left(\partial_r + \frac{1}{r}\right) + (\lambda^2 - 4)\partial_{zz}^2\right]\hat{P} = 0 \tag{22}$$

The wall boundary condition (16) becomes

$$B_w(\hat{P},\hat{\omega}) = 0$$

$$B_w(\hat{P},\hat{\omega}) = \left[n_r\left(\lambda^2\partial_r - \frac{2\lambda}{r}\right) + n_z(\lambda^2 - 4)\partial_z\right]\hat{P} \tag{23}$$

$$+ n_r\lambda(\lambda+1)(\lambda-2)z\hat{\omega} + n_z(1-\lambda)(\lambda^2-4)r\hat{\omega}$$

The free-surface boundary condition (18) becomes

$$B_w(\hat{P},\hat{\omega}) = (Fr^{-2} + \beta^2 r^2)^{-1/2}\lambda^2(\lambda^2 - 4)\hat{P} \quad \text{on} \quad C_f \tag{24}$$

The boundary eigenvalue problem posed by Eqs. (21–24) is solved numerically by a finite element scheme using the method of weighted residuals. In the Galerkin approach, given a set of basis functions $N_i(z,r)$ (typically satisfying homogeneous boundary conditions), we can express the governing equation together with the boundary conditions as

$$\int_A N_i L\hat{P} r \, \mathrm{d}A + a \int_{C_f} N_i[B_w(\hat{P},\hat{\omega}) - (Fr^{-2} + \beta^2 r^2)^{-1/2}$$

$$\times \lambda^2(\lambda^2 - 4)\hat{P}] r \, \mathrm{d}C + b \int_{C_w} N_i B_w r \, \mathrm{d}C = 0 \tag{25}$$

For the mixed-boundary conditions, it is convenient to select the values of the Lagrange multipliers a and b so as to eliminate the derivative terms that appear in the line integrals. By the Green-Gauss theorem, the area integral can be reduced to a lower order form, together with a boundary contribution. For $a = -1$ and $b = -1$, Eq. (25) gives

$$-\int_A [\lambda^2(\partial_r N_i)\partial_r + (\lambda^2 - 4)(\partial_z N_i)\partial_z]\hat{P} r \, \mathrm{d}A$$

$$-\int_A \frac{\lambda^2 N_i}{r^2}\hat{P} r \, \mathrm{d}A + \int_C N_i n_r \frac{2\lambda\hat{P}}{r} r \, \mathrm{d}C + \lambda^2(\lambda^2 - 4)$$

$$\times \int_{C_f} N_i (Fr^{-2} + \beta^2 r^2)^{-1/2}\hat{P} r \, \mathrm{d}C$$

$$-\int_C N_i[n_r\lambda(\lambda+1)(\lambda-2)z$$

$$+ n_z(1-\lambda)(\lambda^2-4)r] r \, \mathrm{d}C\hat{\omega} = 0 \tag{26}$$

where $i = 1$, NN and NN is the number of nodes. Finally, Eqs. (21) and (26) can be expressed as a generalized eigenvalue problem[14] and solved directly for the coupled eigenmodes.

Numerical Analysis

Modal Convergence

In this study a simple spherical chamber geometry is assumed and the equilibrium liquid shape is automeshed with linear triangular finite elements. In Fig. 2, the assumed shape with recirculation gas flow is meshed; the surface without flow is also indicated. In McIntyre and Tanner's[13] original work a somewhat more detailed chamber geometry was manually meshed. Selected values for the two auto-mesher parameters Nr and Nz and the resulting matrix sizes are shown in Table 1. Also tabulated are the resulting liquid mass and nondimensional values for the two dominant liquid-mode frequencies. Numerical convergence of the solution is established by increasing Nr and Nz until the eigenvalue and the norm of eigenvectors change to within less than 1.5%.

One of the major features of the two dominant liquid modes is that they do not show appreciable variation in the axial direction since the pool of liquid is shallow. This pair of modes, aptly termed "swirl" modes, was first identified by McIntyre and Tanner in numerical simulations and confirmed by forced-motion test at Hughes. The retrograde mode swirls in the same direction as, and hence can resonate with, the nutation of a prolate spinning body ($\sigma < 1$). In the next subsection, we shall evaluate the liquid and coupled modes in the case of a pool of liquid under equilibrium spin and thrust without gas flow.

Nutational Stability Without Gas Flow

With the first assumption of constant chamber gas pressure, Fig. 3 shows liquid-mode frequency curves as functions of the reciprocal of the Froude number, Fr^{-1}, for the cases of 9.09 kg (20 lbm) and 27.3 kg (60 lbm) liquid mass. The mass of liquid is used for parameterizing the volume. The density of slag, ρ, used is 2.24 g/cm^3 (140 lbm/ft^3), which is commonly assumed as the density of the aluminum oxide of the solid propellant. The spherical wall radius is scaled to unity, and the radius of the inner cylindrical wall

Table 1 Size of computation and convergence

Nr	Nz	Nodes	Elements	Matrix size	Liquid mass, kg	Prograde frequency	Retrograde frequency
1	1	3	1	13 × 13	19.74	0.3841	−0.4532
3	2	9	8	29 × 29	21.25	0.3905	−0.6287
5	3	18	21	51 × 51	21.37	0.3912	−0.6423
7	4	30	40	79 × 79	21.42	0.3914	−0.6461
9	7	52	77	127 × 127	21.43	0.3915	−0.6476

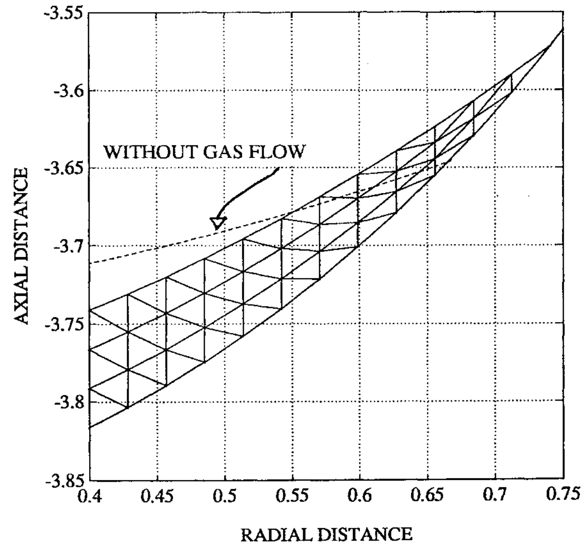

Fig. 2 Slag surface shape and mesh at burnout.

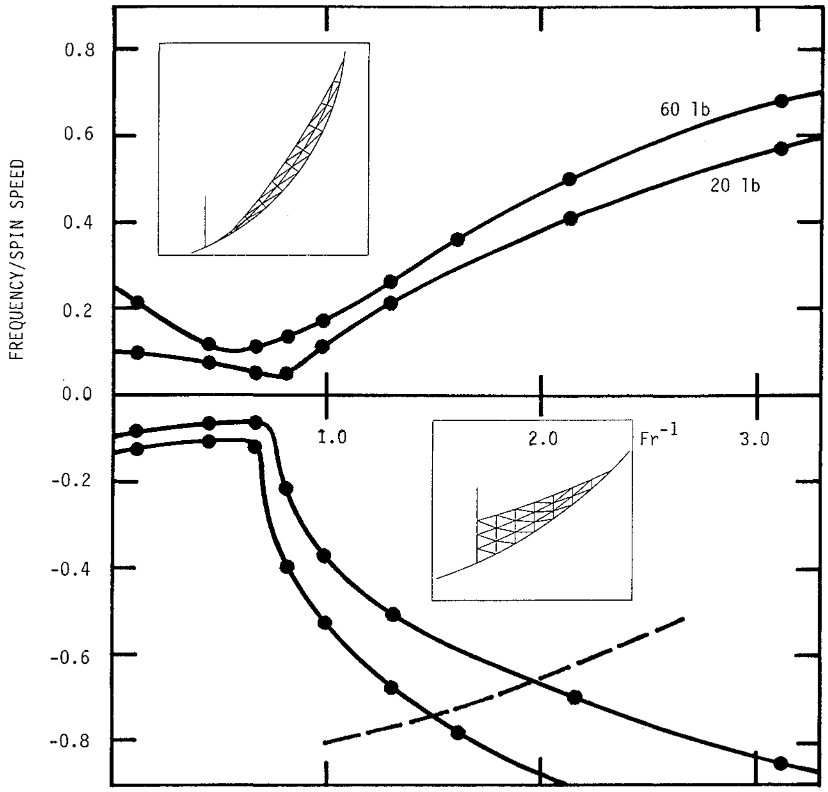

Fig. 3 Natural frequencies of mode pair of interest.

is 0.4, the value we use for the STAR 48 motor. Both the prograde (positive) and retrograde (negative) modal frequencies move toward zero as the ratio of thrust to centrifugal acceleration drops. The curves show a switch in characteristics near $Fr^{-1} = 0.7$, which indicates that the liquid detaches from contact with the submerged nozzle wall as the increasing centrifugal effect throws the liquid outboard. In the smaller mesh diagrams included with the figure, we show these two distinct static liquid conditions. As the liquid mass increases, the frequency of the prograde mode increases and the frequency of the retrograde mode decreases. We also include, in dashed line on Fig. 3, the flight path of the RCA-D spacecraft, indicating the nondimensional body nutation frequency ($\sigma - 1$) as a function of Fr^{-1}. The flight curve crosses the frequency curves of the retrograde mode, suggesting that near the crossing there is a possibility for mode locking.

Figure 4 shows the major stability diagram vs two vehicle parameters: inertia ratio σ and nondimensional axial offset of the slag center of mass (CM) from the vehicle CM, q. The stability boundaries are computed as follows. We vary Fr and find the pair of free-liquid modes as we did for Fig. 3. We then set $\sigma - 1$ in turn equal to the retrograde frequency. This represents the tuned condition where the vehicle nutation frequency and the liquid retrograde mode are equal and hence defines the point of maximum potential for instability. The remaining factor, modal coupling, is then varied and the coupled modes are computed. For the two liquid mass cases this is done by varying the liquid axial offset q. By examination of the coupled nutation root the stable and unstable intervals of q are thus identified. The blank and cross-hatched regions represent the stable and unstable regions, respectively. The stable region implies neutral stability rather than asymptotic stability, since no dissipation has been included.

The two stability boundaries shown for the two different cases of mass of liquid corresponds to 27.3 kg (upper curve) and 9.09 kg (lower curve). The two boundary curves do not cross each other. The RCA-D flight path is also shown in dashed line, for comparison. With 27.3 kg of slag it is seen that instability is predicted just at the end of burn. This is quite promising for the slag hypothesis. However, in fact, exponential nutation growth was observed toward the last third burn time of the actual RCA-D flight. The hydrodynamic model excluding gas mean flow does not reproduce the data as well as desired. Before addressing this issue, we make some further remarks about Fig. 4.

In computing the stability boundaries, the truncation parameters of the solutions are between $Nr = 7$ and $Nz = 4$ and $Nr = 12$ and $Nz = 3$. The results are accurate to within 1.5%. The stability characteristics reverses across the lines of $\sigma = 1$ and $q = 0$. Across these lines, we expect the role of the two competing forces, the thrust and the centrifugal force, to also reverse. Note the similarity between this stability diagram and the one from a planar pendulum model (Fig. 2 in Ref. 5). This similarity is no coincidence since both models have the same number of physical forces. The unstable regions for negative q are of particular interest in the cases of the PAM-D spacecraft. Previous dynamical models[2,4,6,8] appear to focus on the thrust as the primary destabilizing force, whereas this diagram suggests that, for $\sigma < 1$, the spin force always destabilizes but the thrust stabilizes for $q < -1$ and destabilizes for $0 > q > -1$. The roles of the two forces reverse for $\sigma > 1$. The destabilizing force only overcomes the stabilizing force for parameters in the cross-hatched areas. In fact, McIntyre and Tanner,[13] using an earlier hydrodynamic model, were the first investigators to suggest that thrust is stabilizing in the case of PAM-D. In the stability diagram, the modal characteristics of the two modes of interest change in the range between $\sigma = 0.9$ and 1.1, where a transition of liquid shape due to the detachment from the inner wall has occurred. This portion of the stability boundary is indicated by a dashed line.

The hydrodynamic model results without gas flow suggest that, although nutation locking when the liquid pool lies below the dry body's center of mass is possible, under a high-thrust situation like those in the PAM-D flights, the spin effect is simply not strong enough to overcome the stabilizing effect of thrust acceleration. It has been argued by others that a simple hydrodynamic liquid model may not be sufficient because the effect of gas flow above the liquid is not included. Most analysts agree, however, that the onset of instability cannot reasonably depend on finite-amplitude disturbances, given the consistent character of the flight data. Therefore, we believe that, in order to improve our comparison with flight data, the basic equilibrium state of the linearized hydrodynamic liquid model

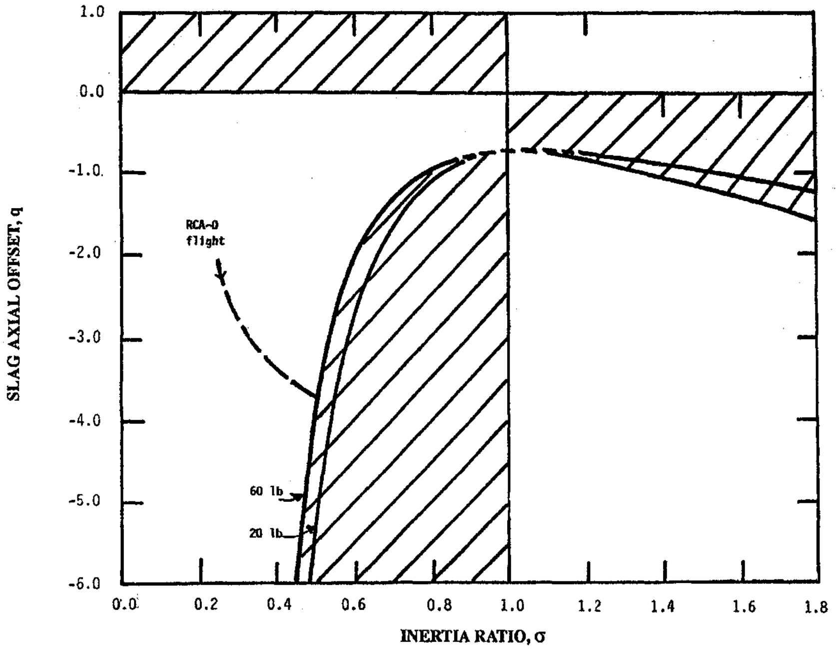

Fig. 4 Stability diagram in the σ-q plane.

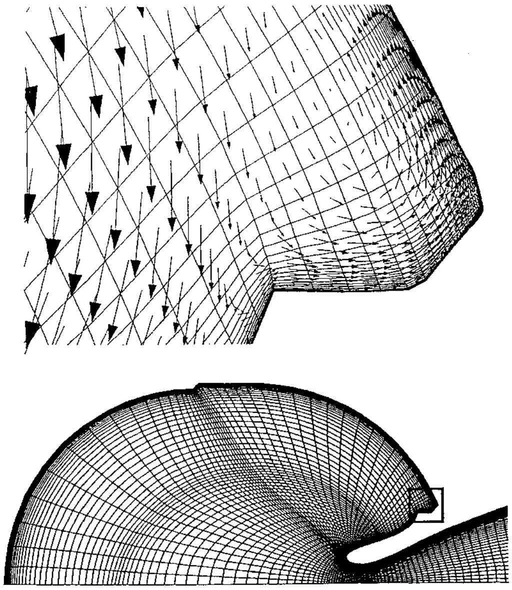

Fig. 5 Recirculation gas vortex over slag region. (From Ref. 3, Figs. 26 and 27. Reproduced with permission of Aerospace Corp.)

may have to be modified to some extent. In the next subsection, a simulation of the PAM-D flight is presented in which the effect of gas flow is introduced to address this issue.

Nutational Stability with Recirculating Gas Flow

Figure 2 shows the mesh section of the liquid in our simulation that corresponds to the 85th s of burn. The value of β in this case is 1.9. We allow both a drag force and a normal force to be exerted on the liquid surface due to the flow of a gas recirculation vortex. The drag force is due to friction, and the normal force is due to the centrifugal pressure of the vortex. The existence of a recirculation vortex has indeed been confirmed by a numerical experiment on the chamber flow.[3] Figure 5 shows the rocket motor geometry of Misterek et al.[3] (similar to the configuration we used) and a portion boxed. The boxed region is where the liquid lies and there exists a recirculation flow.

In the simulation, we again use a typical flight history of a PAM-D spacecraft. The time history of major parameters is shown in Tables 2 and 3. Fixed parameters are: spin speed, 30 rpm; thrust level, 71,400 N; chamber radius, 0.61 m; emerged nozzle length, 0.61 m; submerged nozzle length, 0.23 m. These lengths are measured from the liquid mass center. For simplicity, we assume the slag mass to be accumulated linearly in time. The time history of Fr, σ, and ϵ are constrained by flight data. In matching the flight data, we adjust β. From the flight data, we estimate the onset of growth occurred at about the 57th second and lasted until burnout. In Table 3 we choose several instants of time at which the coupled hydrodynamic problem is solved and the coupled eigenvalues are reported. The inner cylindrical wall is at 0.4 times the spherical radius from the axis. In Fig. 6, we show the simulated growth rate in time. The solid curve represents the net growth rate assuming the presence of jet damping.[15] The jet-damping growth rate λ_J is negative and is assumed to be governed by the expression

Table 2 Mass properties of RCA-D during burn

Time, s	Axial MOI, kg-m^2	Transverse MOI, kg-m^2	Dry mass, kg	From CM to nozzle exit, m	σ	Fr^{-1}	ϵ
0	716.8	2901.6	3252.9	1.92	0.247	0.910	0.0655
10	676.7	2651.8	3016.1	2.03	0.255	0.981	0.0717
20	636.5	2402.0	2779.4	2.14	0.265	1.065	0.0792
30	596.4	2152.2	2542.7	2.25	0.277	1.164	0.0883
40	556.2	1902.3	2306.0	2.37	0.292	1.284	0.0999
50	516.0	1652.6	2069.2	2.47	0.312	1.430	0.1150
60	475.8	1402.8	1832.5	2.59	0.339	1.615	0.1355
70	435.7	1153.0	1595.8	2.70	0.378	1.855	0.1649
80	395.5	903.2	1359.1	2.81	0.438	2.178	0.2105
85	375.5	778.3	1240.7	2.87	0.483	2.386	0.2443

$$\lambda_J = -C(t)\dot{m}\left(l_2^2 - l_1^2\right)/A\Omega \tag{27}$$

where $\dot{m}$ is the uniform gas flow rate, which can be computed from Table 2 by dividing the burned mass by the burn time; l_1 is the average distance between the center of mass of the vehicle and the solid propellant; and l_2 is the distance between the center of mass and the nozzle exit. In this model we introduce a coefficient $C(t)$ equal to $1.0 - 0.4t/85$. The dotted curve in Fig. 6 represents the resonant growth rate with no jet damping. No viscous damping is assumed. The smooth advent at $t = t_a$ is due to the interpolation effect. Theoretically, at that point the growth rate varies as $(t - t_a)^{1/2}$ as t increases from t_a. The time evolution of growth rate as shown is consistent with observations and reconstructions from flight teleme-

Table 3 Simulation parameters for latter part of burn

Time, s	55	60	65	75	85
Fr^{-1}	1.52	1.62	1.73	2.00	2.18
β	1.60	1.60	1.60	1.85	1.90
Slag mass, kg	18.2	19.5	20.9	23.9	27.2
σ	0.33	0.34	0.36	0.40	0.49
ϵ	0.125	0.136	0.149	0.185	0.244
Free liquid Frequency	−0.5434	−0.5965	−0.6507	−0.7160	−0.7882
Coupled liquid Frequency	−0.6832 −0.5727	−0.6517 $\pm 0.0169i$	−0.6757 $\pm 0.0470i$	−0.7122 $\pm 0.0742i$	−0.7404 $\pm 0.0556i$

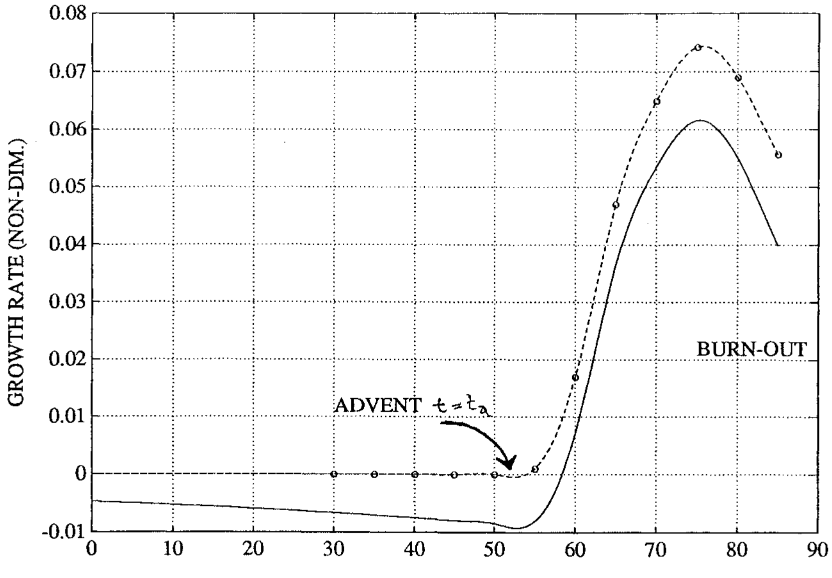

Fig. 6 Simulated growth rate (——) with and (- - - -) without jet damping.

try data (see Ref. 2). The same time evolution of growth rate has been constructed from the pendulum model also.[5] In Fig. 7, we show the frequencies of the two interacting modes. The rising and decreasing dotted curves respectively represent the free-body nutation frequency ($\sigma - 1$) and the free-liquid frequency. The two curves cross each other near the 64th second of burn. The two solid curves represent the coupled frequencies. To the left, the solid curves approach the dotted curves asymptotically as time decreases, indicating decoupling. Near the crossing point, however, the two coupled modes coalesce at about the 58th second and merge until burn-out. The merged coupled frequency remains closer to the free-liquid frequency rather than to the free nutation frequency. In Fig. 8, we use the growth rate and frequency time history to construct the temporal behavior of the transverse rate. In complex notation of Eq. (17), we have

$$\dot{\omega} = (\lambda_J + \lambda_r + i\lambda_i)\omega$$

where λ_r and λ_i are respectively the growth rate and the coupled frequency, which are available in the form of time series. The time series of the transverse rate is given by

$$\omega = \omega_0 \exp\left[\int_0^t (\lambda_J + \lambda_r + i\lambda_i)\, dt\right] \tag{28}$$

In Fig. 8, we use $\omega_0 = 0.8$ deg/s; the spin speed is 60 rpm. After 85 s of burn, we turn off the growth rate and maintain a constant amplitude and frequency thereafter. A matched telemetry time history of the PAM-D spacecraft was shown in the paper by Or[5] and will not be reproduced here. The simulation compares reasonably well.

In the pendulum model,[5] we used a pendulum mass of roughly one-tenth of the current liquid mass. In Ref. 5 and present simulations we allow the mass to increase linearly with time. We have to add a weighing factor $K \approx 10$ to the cross-coupling terms in the pendulum model [see Ref. 5, Eq. (20)] to decrease the pendulum amplitude since at $K = 1$ the pendulum amplitude becomes artificially large for a few degrees of nutation angle. The relative importance given to the two cross-coupling matrices in the case of the mechanical model is clearly deficient, as far as the PAM-D flight simulation is concerned. From examination of the unstable coupled eigenvector this deficiency is eliminated with the hydrodynamic model since the maximum nondimensional surface elevation

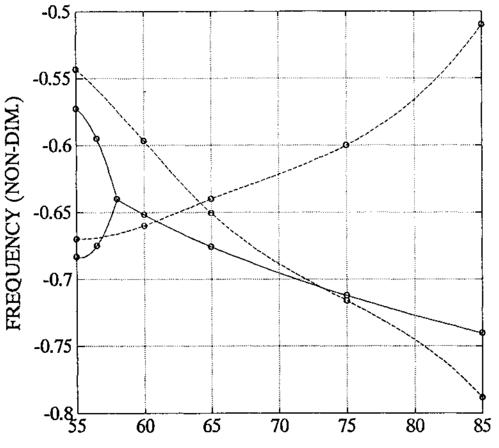

Fig. 7 Mode frequencies: coupled; free liquid (decreasing dashed line); free nutation (increasing dashed line).

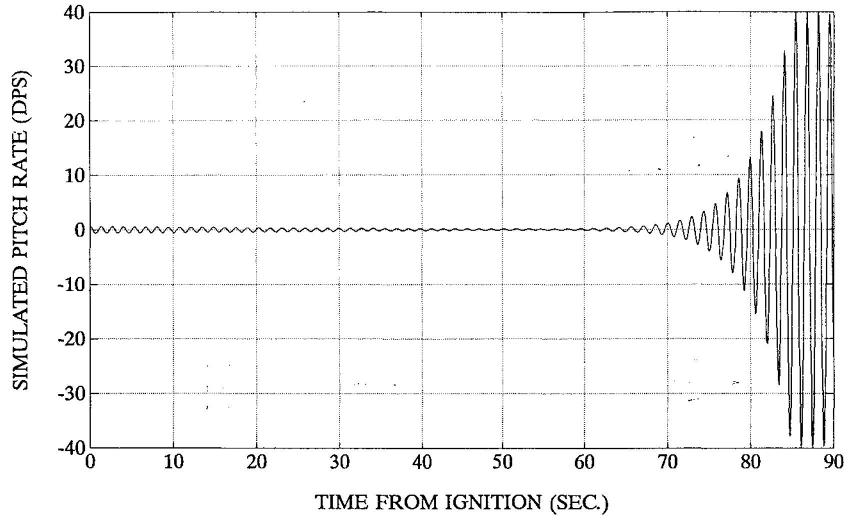

Fig. 8 Simulation of spacecraft transverse rate.

in this case is 0.08 at a nutation angle of 5 deg. This amplitude of surface deformation is reasonable for the PAM-D bowl configuration. Also from the eigenvector at resonance, the reduced-pressure amplitude and, hence, surface deformation are maximum at the inboard location and their phase leads transverse rate by 36 deg; the outboard amplitude and phase lead decrease by 4:1 and 2:1, respectively.

Conclusion

The stability of a symmetric spinning body containing a trapped shallow pool of liquid at equilibrium in the aft part of a rocket motor chamber is studied using a linearized hydrodynamic coupled finite element model. The hydrodynamic problem is assumed to be both incompressible and nondissipative, which essentially means that the liquid disturbance torque is caused by pressure. The assumption that the mass of liquid is significantly smaller than that of the rigid body has also been made and is reasonable. A pair of liquid "swirl" modes is found, one prograde and the other retrograde relative to the body, in agreement with earlier unpublished numerical and experimental results. The frequency of the retrograde mode intersects vehicle nutation frequency during the latter part of the flight. Both modes characteristically exhibit no dynamic pressure variation along the axial direction.

The coupled stability is first studied for no gas flow, $\beta = 1$. Results show that the stability is controlled by the two major parameters, σ and q. The resonance condition restricts the value of Fr. For $\sigma < 1$, the gravity or thrust destabilizes for $q > 0$ and stabilizes for $q < 0$; on the other hand, the spin effect always destabilizes. For $\sigma > 1$, the role of gravity reverses with respect to the sign of q, and spin always stabilizes in this case. Since the PAM-D chamber aft dome is to the rear of the center of mass of the rigid body ($q < 0$), in order for a prolate rigid body to become unstable, the destabilizing spin effect has to overcome the stabilizing gravity effect. This requires the centrifugal force to have a long moment arm, i.e., a large negative q. Furthermore, the liquid has to push more against the side wall rather than to the bottom wall so as to generate a larger *destabilizing* radial pressure force than a *stabilizing* axial force. We anticipate that a hydrodynamic liquid model without gas flow has all the important destabilizing effects included. The only shortcoming is that the flight path does not enter the predicted unstable region soon enough.

In the second model, jet damping and the effect of internal gas flow on the equilibrium shape of the liquid slag are considered. A free parameter β is used to adjust the free-surface shape and reproduce the flight growth rate. The cause of this needed change in shape is a recirculation gas flow, whose qualitative effect on the liquid can be argued to produce an effect similar to our beta assumption. The existence of a recirculation vortex has in fact been confirmed in numerical experiment, and its qualitative effect on the liquid is to push the liquid outboard. Determination of the quantitative equilibrium liquid shape requires further analyses; however, only a small change appears to be needed to crucially alter the force balance.

Many authors appeared to be aware of one deficiency in the pendulum model, namely, the artificially large pendulum amplitude for a few degrees of nutation angle. We remarked earlier that this problem is due to the wrong relative strength of the cross-coupling terms, rather than to a neglect of nonlinearity. This problem appears to be overcome by the present model. Also a much more reasonable result, as far as slag displacement or surface deformation height of the liquid, is reported. However, the increase in coupled nutation frequency during the burn is inconsistent with flight observation and the trend of free vehicle frequency. Further improvements in characterizing the slag condition are still needed. However, the significant potential for slag slosh to destabilize nutation is apparent.

It is also noted that if a solid rocket motor is inserted in an oblate spinning spacecraft (i.e., $\sigma > 1$), the possibility of nutational instability is still not avoided; the major-axis stability rule is not applicable under thrust.

Acknowledgments

This study was supported by Hughes Aircraft Company IR&D. The authors also acknowledge Patrick Yip for his assistance in the computations and thank the anonymous reviewers for their detailed and helpful suggestions regarding the content and presentation of this work.

References

[1] Miller, M. C., "Flight Instabilities of Spinning Projectiles Having Nonrigid Payloads," *Journal of Guidance, Control, and Dynamics*, Vol. 5, No. 2, 1982, pp. 151–157.

[2] Flandro, G. A., Leloudis, M., and Roach, R., "Flow-Induced Nutation Instability in Spinning Solid Propellant Rockets," Astronautics Laboratory (AFSC), AL-TR-89-084, April 1990.

[3] Misterek, J., Murdock, J. W., and Koshigoe, S., "The Analysis and Simulation of the PAM-S Coning Instability," Aerospace, TOR-0091(6464-06)-1, 1990, Vol. 4; also "Gas Dynamic Flow in a Spinning Coning Solid Rocket Motor," *Journal of Propulsion*, Vol. 9, No. 1.

[4] Mingori, D. L., and Yam, Y., "Mutational Instability of a Spinning Spacecraft with Internal Mass Motion and Axial Thrust," *Proceedings of the AIAA Astrodynamics Conference* (Williamsburg, VA), AIAA, Washington, DC, 1986, pp. 367–375; also AIAA Paper A86-47901.

[5] Or, A. C., "Rotor-Pendulum Model for the Perigee Assist Module Nutation Anomaly," *Journal of Guidance, Control, and Dynamics*, Vol. 15, No. 2, 1992, pp. 297–303.

[6] Cochran, J. E., Jr., and Kang, J. Y., "Nonlinear Stability Analysis of the Attitude Motion of a Spin-Stabilized Upper Stage," AAS/AIAA Spaceflight Mechanics Meeting, Houston, TX, Paper AAS 91-109, Feb. 1991.

[7] Kang, J.-Y., and Cochran, J. E., Jr., "Further Investigations of Anomalous Attitude Motion of Spin Stabilized Upper Stages," AAS/AIAA Astrodynamics Specialist Conference, Durango, CO, Paper AAS 91-480, Aug. 1991.

[8] Halsmer, D., and Mingori, D., "The Passive Coning Attenuator (PCA): Internal Mass Motion and Axial Thrust Combine to Produce Asymptotic Nutational Stability," AIAA Paper 92-4544, Aug. 1992.

[9] Staunton, B. D., and Mingori, D. L., "Attitude Dynamics of Spinning Rockets in Space with Internal Fluid Motion,"AIAA Paper 93-3758, Aug. 1993.

[10] Greenspan, H. P., *The Theory of Rotating Fluids*, Cambridge Univ. Press, Cambridge, England, UK, 1968.

[11] Meyer, R. X., "In-Flight Formation of Slag in Spinning Solid Propellant Rocket Motors," *Journal of Propulsion and Power*, Vol. 8, 1992, pp. 45–50.

[12] Stewartson, K., "On the Stability of a Spinning Top Containing Liquid," *Journal of Fluid Mechanics*, Vol. 5, 1959, pp. 577–592.

[13] McIntyre, J. E., and Tanner, T. M., "Fuel Slosh in a Spinning Propellant Tank: An Eigenmode Approach," *Space Communication and Broadcasting*, Vol. 5, 1987, pp. 229–251.

[14] Or, A. C., and Challoner, A. D., "Stability of a Liquid-Filled Spinning Top: A Numerical Approach," *Journal of Sound and Vibration*, Vol. 175, No. 1, 1994, pp. 17–37.

[15] Thomson, W. T., and Reiter, G. S., "Jet Damping of a Solid Rocket: Theory and Flight Results," *AIAA Journal*, Vol. 3, 1965, p. 413.